Supporting Information

Ionic organic cage-encapsulating phase-transferable metal clusters

Su-Yun Zhang,[a] Zdravko Kochovski,[c] Hui-Chun Lee,[a] Yan Lu,[c,d] Hemin Zhang,[e] Jie Zhang,[a] Jian-Ke Sun,*[a] and Jiayin Yuan*[b]

[a] MOE Key Laboratory of Cluster Science, Beijing Key Laboratory of Photoelectronic/Electrophotonic Conversion Materials, School of Chemistry and Chemical Engineering, Beijing Institute of Technology, Beijing, P.R. China.

[b] Department of Materials and Environmental Chemistry, Stockholm University, 10691 Stockholm, Sweden.

[c] Soft Matter and Functional Materials, Helmholtz-Zentrum Berlin für Materialien und Energie, Hahn-Meitner-Platz 1, 14109 Berlin, Germany.

[d] Institute of Chemistry, University of Potsdam, 14469 Potsdam, Germany.

[e] School of Energy and Chemical Engineering, Ulsan National Institute of Science & Technology (UNIST), Ulsan 689-798, Republic of Korea.

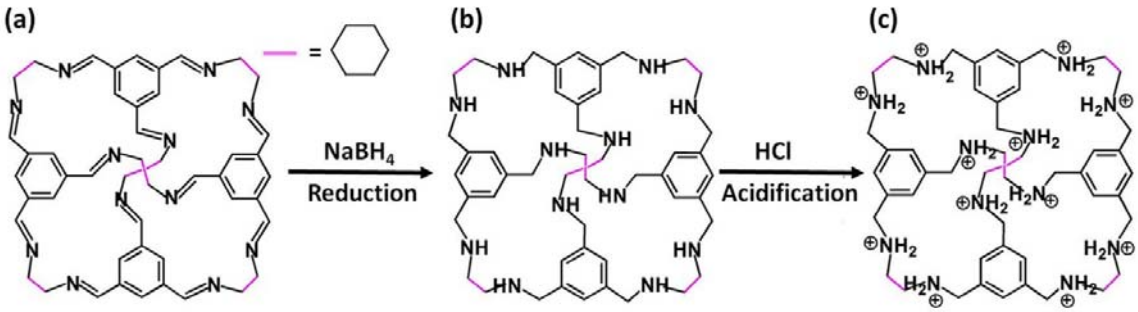

Scheme S1. Scheme illustrating the procedure to prepare the ionic organic cage (I-Cage) from its CC3 precursor, (a) CC3, (b) R-CC3, and (c) I-Cage-Cl (The Cl^- counter anions are omitted for clarity).

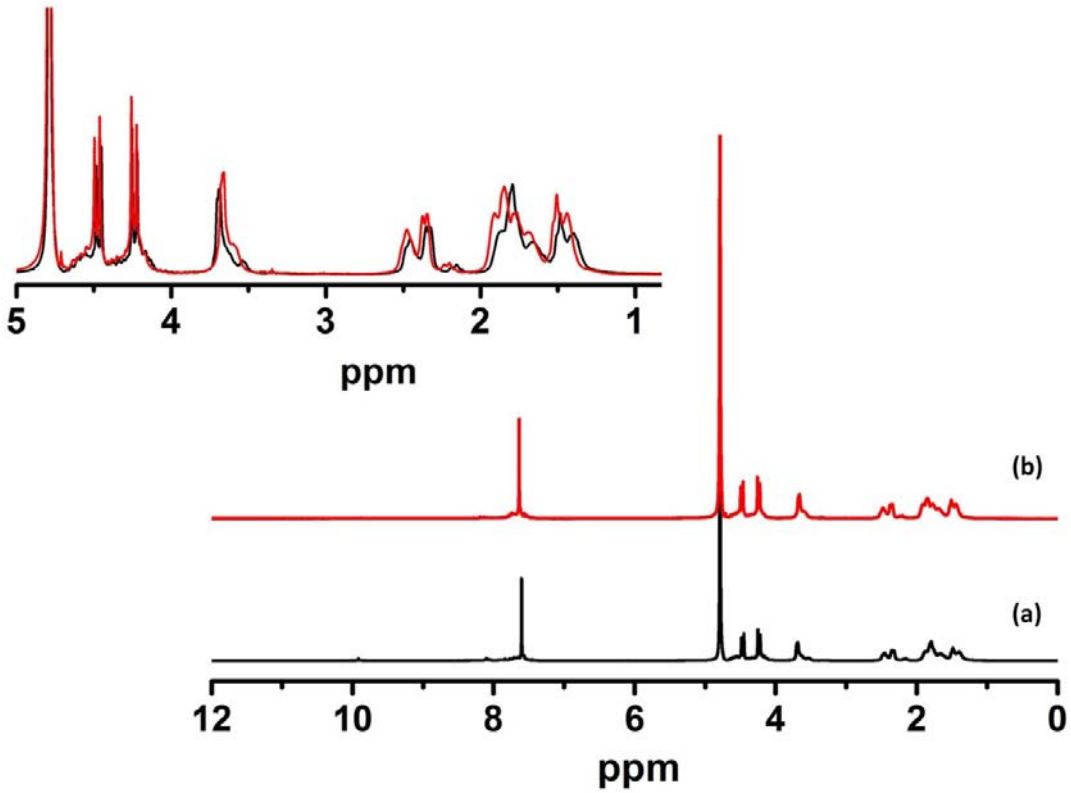

Figure S1. Chemical structures and ^{1}H-NMR spectra of (a) I-Cage-Cl (The integration of the spectrum can be referred in Figure S38) and (b) Au@I-Cage-Cl in D_2O. The inset on the top left shows the comparison between I-Cage-Cl and Au@I-Cage-Cl.

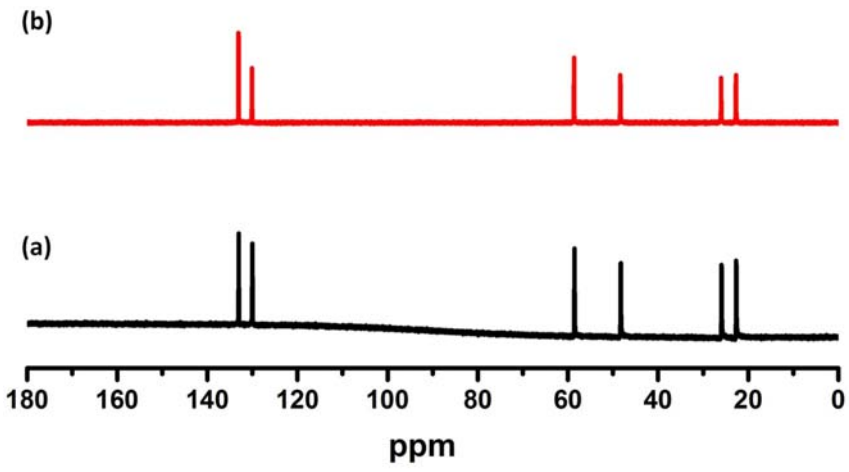

Figure S2. ^{13}C-NMR spectra of (a) I-Cage-Cl and (b) Au@I-Cage-Cl in D_2O.

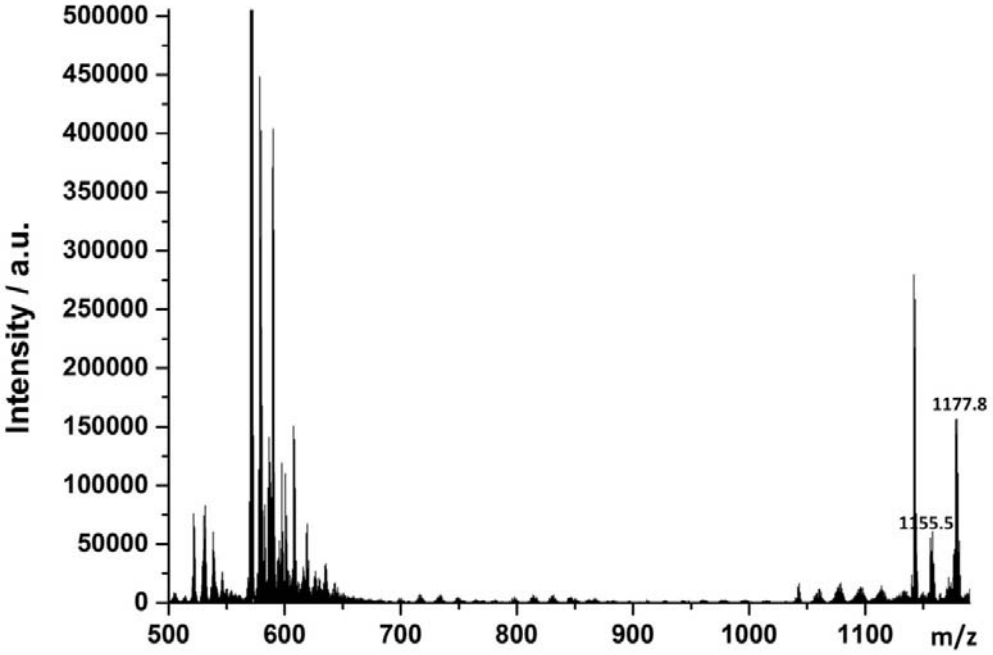

Figure S3. ESI(+)-MS spectrum of I-Cage-Cl, selected $[M+H]^+$ at m/z 1155.5 and selected $[M+Na]^+$ at m/z 1177.8 are marked in the picture.

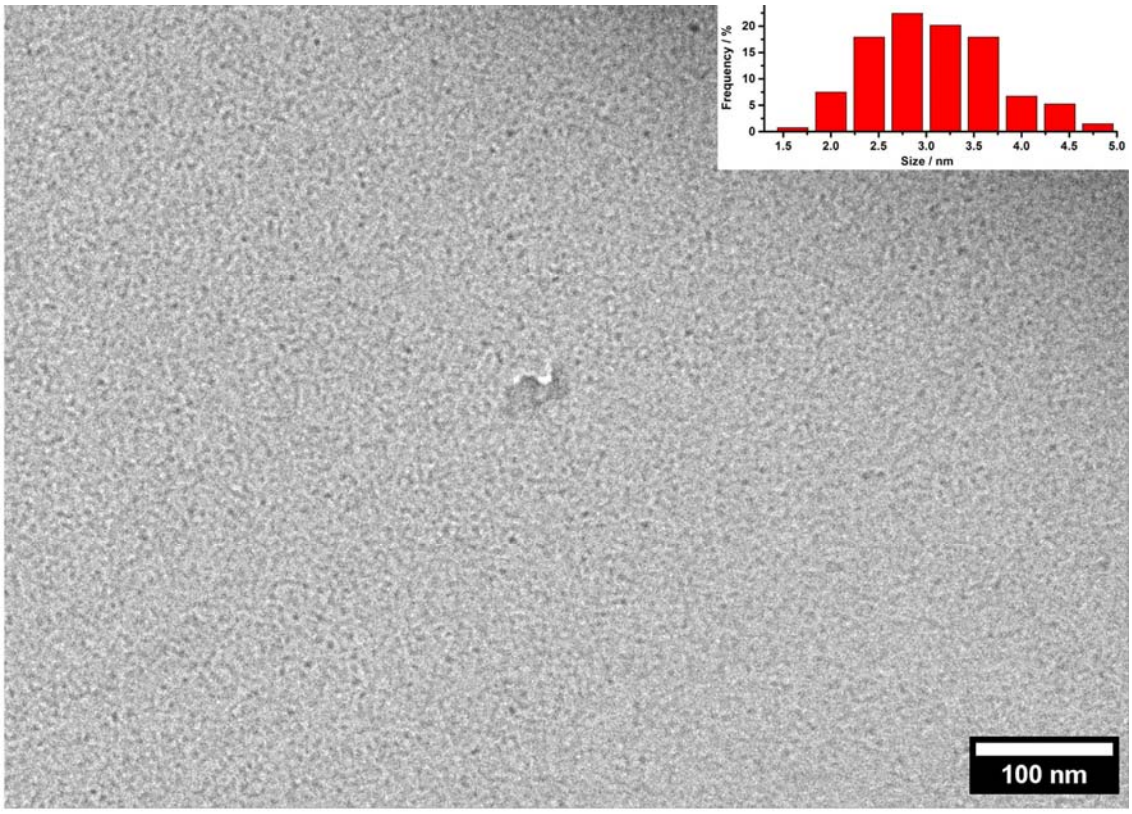

Figure S4. Cryo-EM image of the I-Cage-Cl (dark dot) on a Lacey carbon grid. The inset is the corresponding size distribution histogram of I-Cage-Cl.

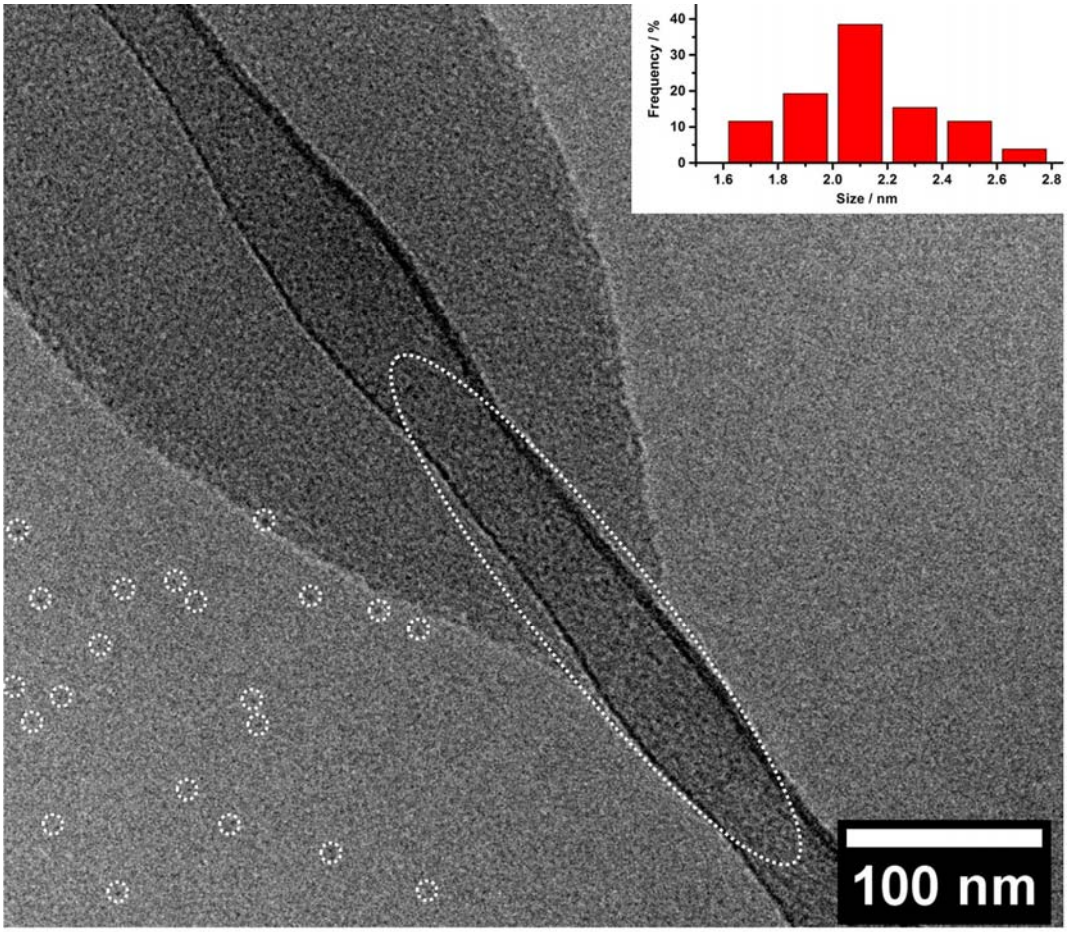

Figure S5. Cryo-EM image of the neutral RCC3 Cage (some dots highlighted by white circles) on a Lacey carbon grid. There are also a large number of RCC3 cage on Lacey carbon (highlighted by white dotted ellipses). The inset is the corresponding size distribution histogram of RCC3 cage.

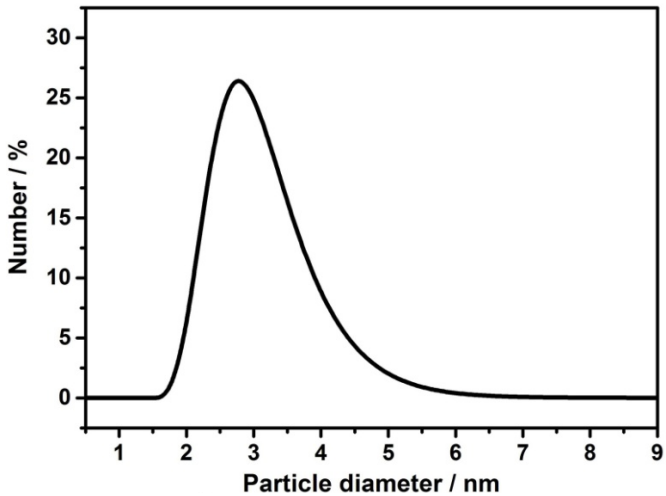

Figure S6. The number-average size distribution of the Au@I-Cage-Cl in aqueous solution observed by DLS.

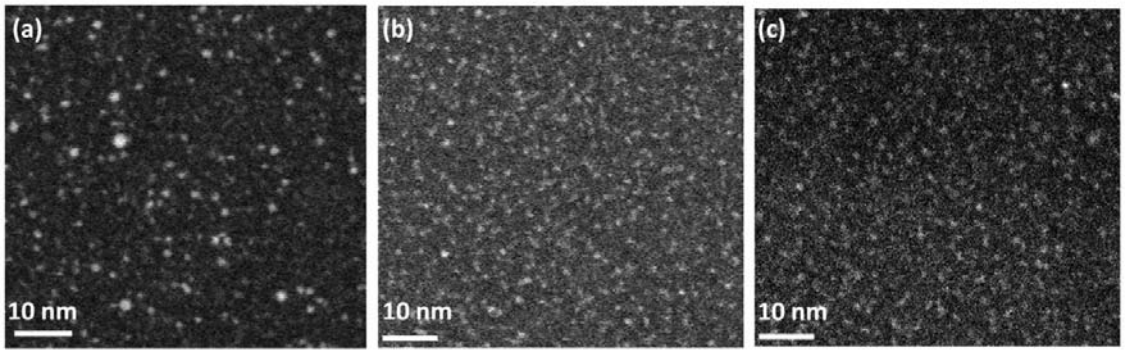

Figure S7. The HAADF-STEM images of (a) Au, (b) Pd and (c) Pt clusters in aqueous solution.

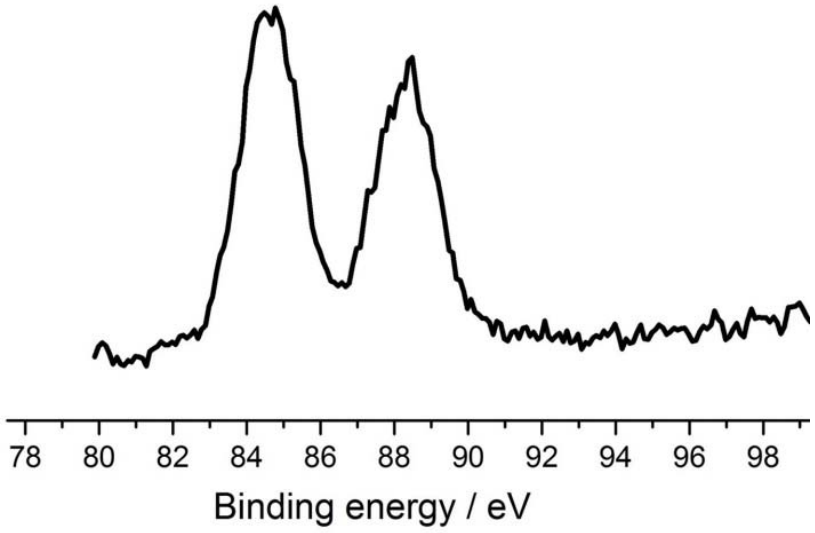

Figure S8. XPS spectrum of Au@I-Cage-Cl showing Au $4f_{7/2}$ (84.4 eV) and $4f_{5/2}$ (88.4 eV) peaks of metallic Au.

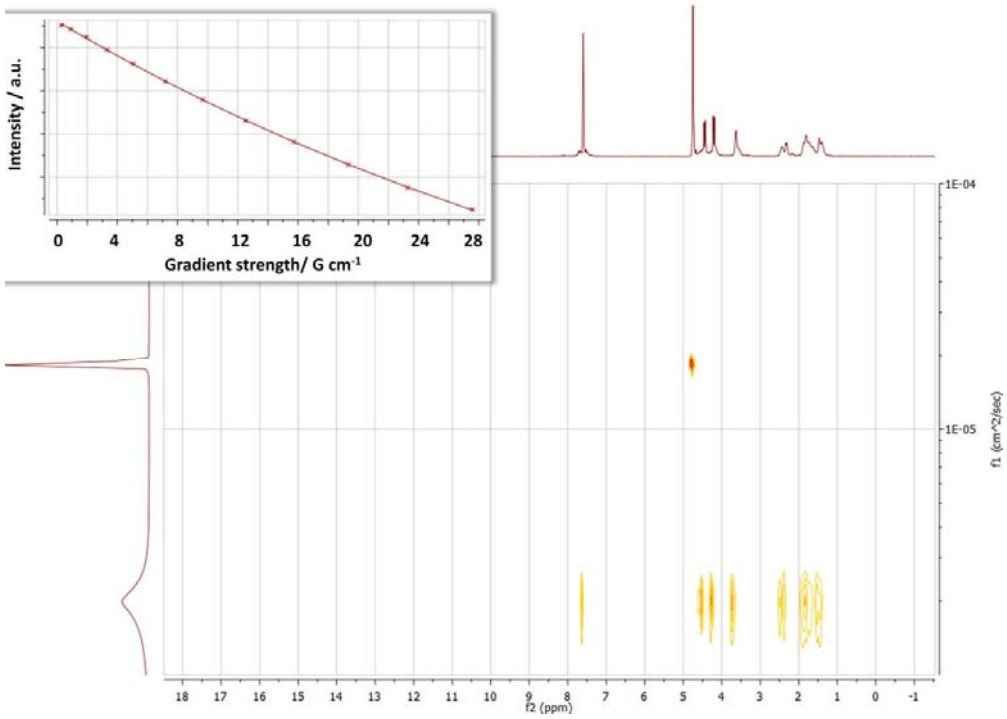

Figure S9. ^{1}H 2D-DOSY NMR spectrum of I-Cage-Cl in D_2O. The inset in upper left is the plot of the signal intensity as a function of the gradient strength. Diffusion coefficients are obtained by non-linear fitting of the decay curve.

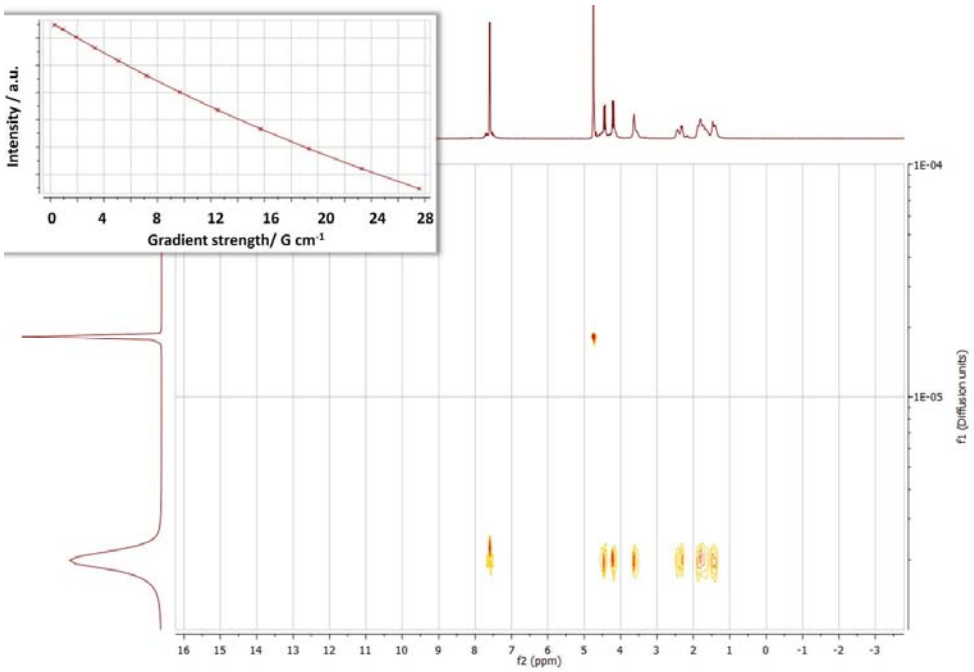

Figure S10. ^{1}H 2D-DOSY NMR spectrum of Au@I-Cage-Cl in D_2O. The inset in upper left is the plot of the signal intensity as a function of the gradient strength. Diffusion coefficients are obtained by non-linear fitting of the decay curve.

Note: The two diffusion coefficients were calculated using the peaks at 7.62 ppm for I-Cage-Cl and Au@I-Cage-Cl. These two peaks are well separated from other resonances, so they are described by a mono-exponential function. Data were analysed by plotting the signal intensities (areas) as a function of the gradient strength, followed by non-linear fitting of the resulting decay curves. For internal consistency, we checked the method by calculating the diffusion for D_2O, which was used as a solvent, from the peak at 4.79 ppm: the diffusion coefficient value $D(D_2O) = 1.84\times10^{-5}$ cm^2 s^{-1} obtained is in agreement with that of D_2O reported in literature.(*J. Phys. Chem.*, 1965, 69, 4412–4412). The diffusion coefficient for I-Cage-Cl was measured as $D(\text{I-Cage-Cl}) = 2.06\times10^{-6}$ cm^2 s^{-1} and for Au@I-Cage-Cl as $D(\text{Au@I-Cage-Cl}) = 2.16\times10^{-6}$ cm^2 s^{-1}.

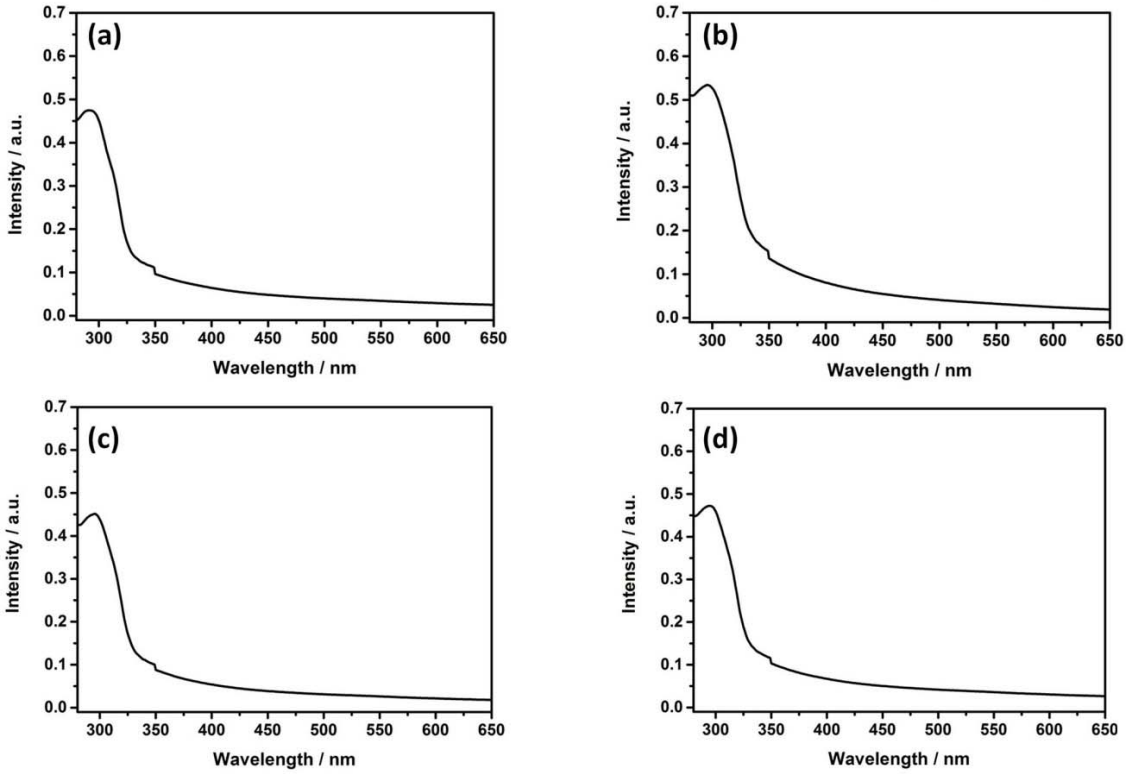

Figure S11. UV-vis spectra of Au cluster after staying in (a) acid, (b) base, (c) heat-treatment at 363 K and (d) liquid N_2.

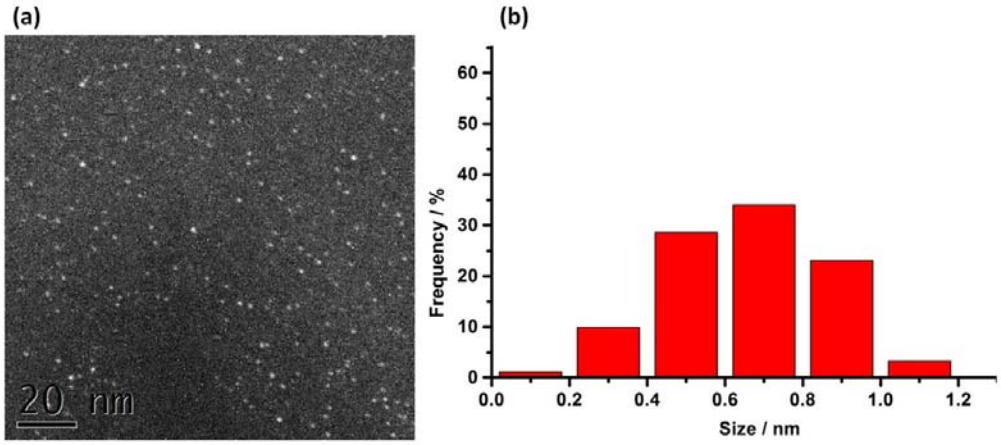

Figure S12. (a) HAADF-STEM image of Au clusters in an acid solution (pH=3) and (b) the corresponding size distribution histogram of Au clusters.

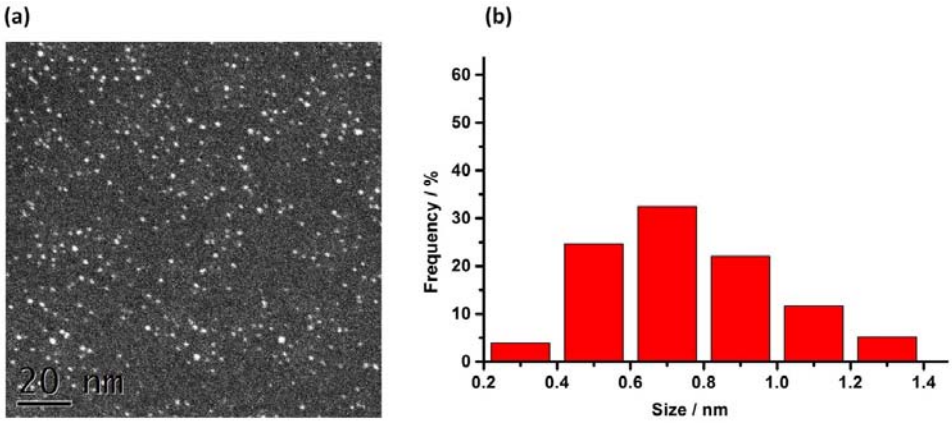

Figure S13. (a) HAADF-STEM image of Au clusters in a base solution (pH=10) and (b) the corresponding size distribution histogram of Au clusters.

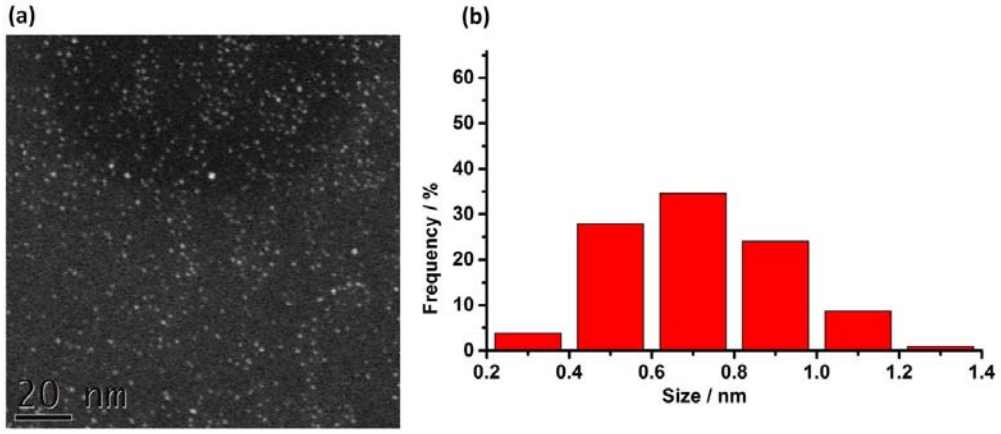

Figure S14. (a) HAADF-STEM image of Au clusters after treated by liquid nitrogen and (b) the corresponding size distribution histogram of Au clusters.

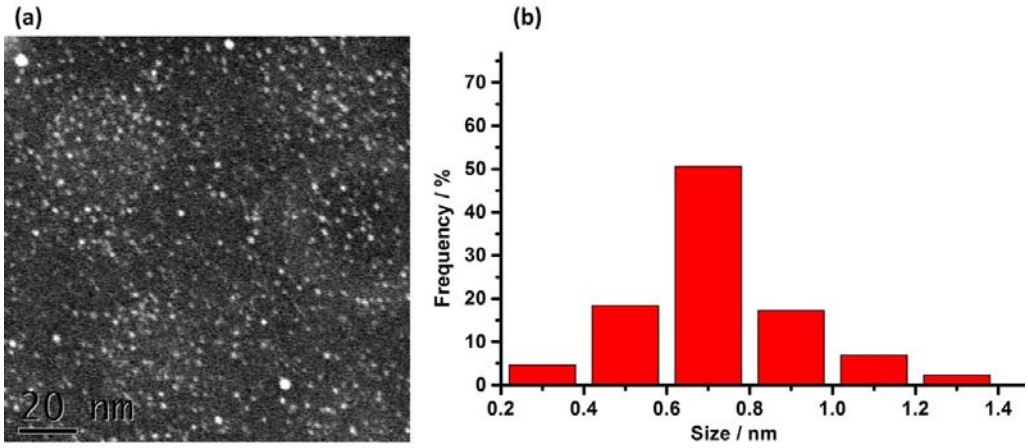

Figure S15. (a) HAADF-STEM images of Au cluster after heat-treatment at 363 K and (b) the corresponding size distribution histogram of Au clusters.

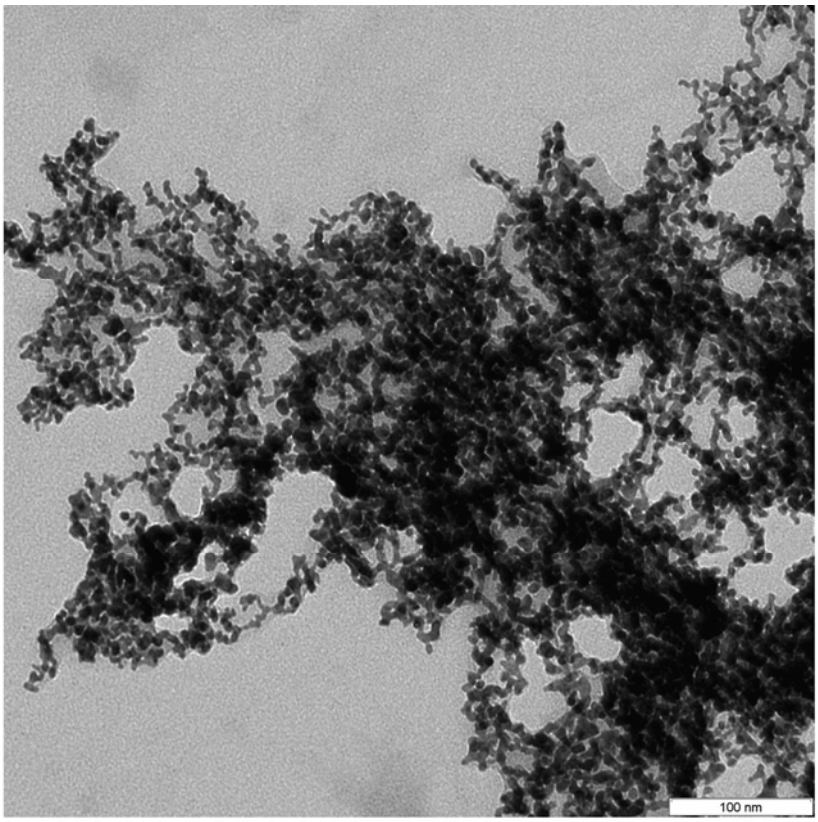

Figure S16. TEM image of Au nanoparticles produced without any support.

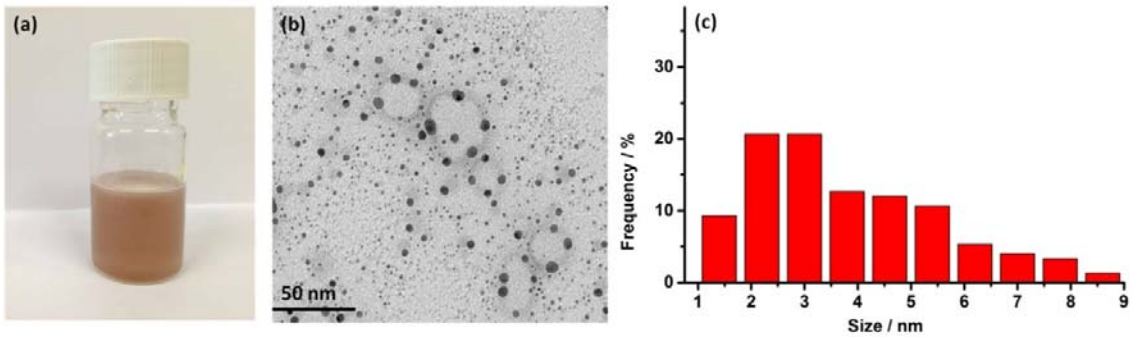

Figure S17. (a) Photograph of Au/RCC3 solution. (b) TEM image of Au/RCC3 and (c) the corresponding size distribution histogram of Au nanoparticles (4 ± 0.8 nm).

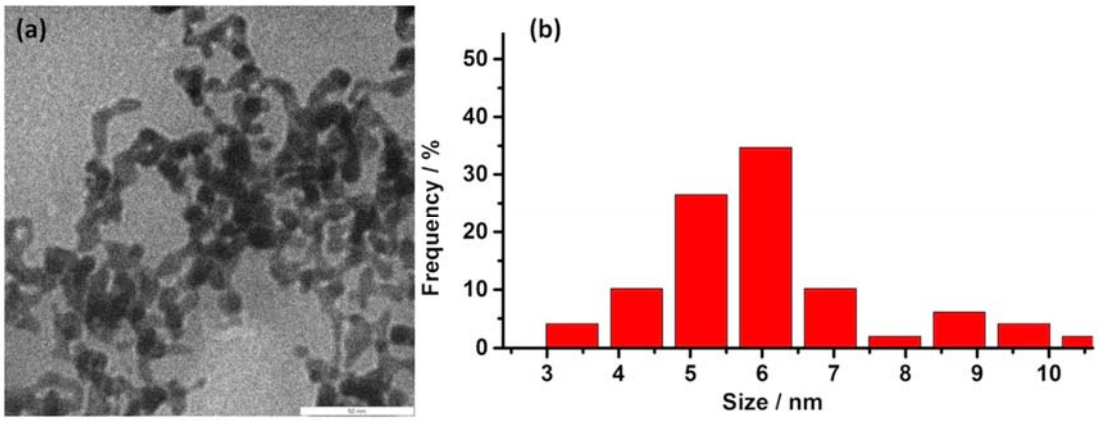

Figure S18. (a) TEM image of Au/4-cyanomethyl-1-vinyl-imidazolium bromide and (b) the corresponding size distribution histogram of Au nanoparticles (6 ± 0.9 nm).

Phase transfer process	**Amount of Au (mg/L, ppm) left in mother phase**
From aqueous to EA phase	4.5 (in aqueous phase)
From EA to aqueous phase	<1 (in EA phase)

Figure S19. ICP-OES result of Au metal left in the mother phase after phase-transfer process.

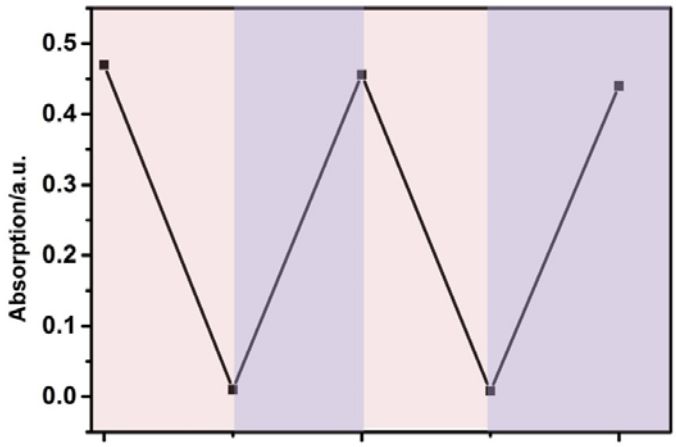

Figure S20. Reversible transfer of Au-I-Cage-Cl (absorbance at 300 nm) in water upon alternating addition of LiTFSI (pink rectangle) and KCl (violet rectangle).

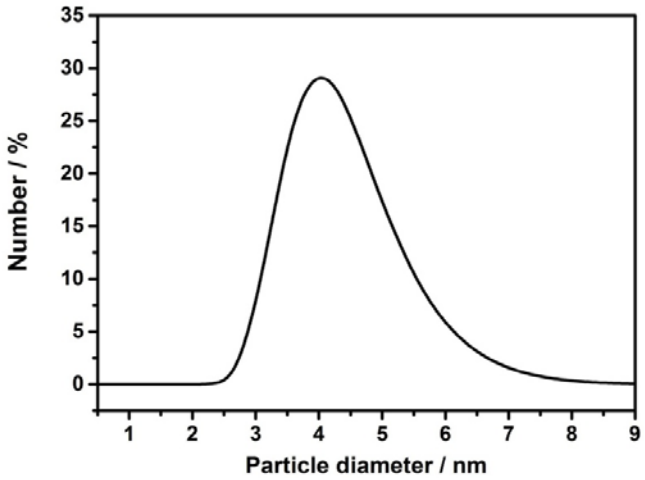

Figure S21. The number-average size distribution of the Au@I-Cage-TFSI in EA solution observed by DLS.

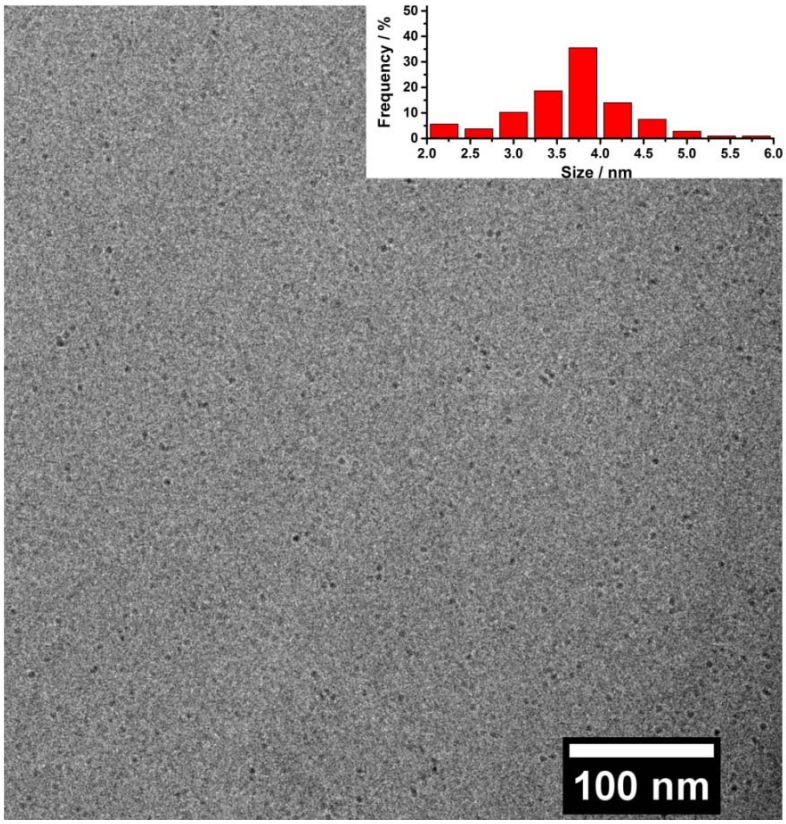

Figure S22. Cryo-EM image of Au@I-Cage-TFSI on a Lacey carbon grid and the size distribution histogram as inset.

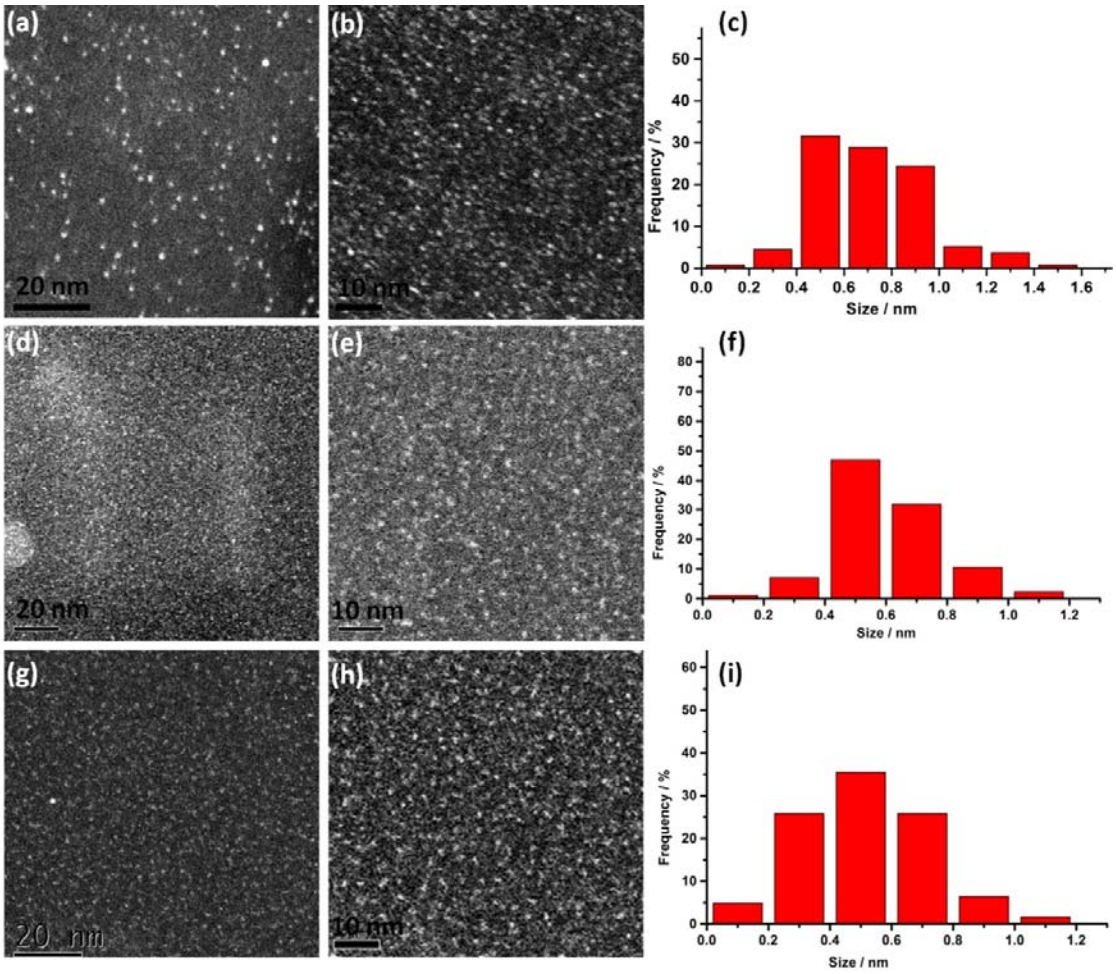

Figure S23. HAADF-STEM images at different magnifications and their corresponding size distribution of Au (a-c), Pd (d-f) and Pt (g-i) clusters in EA solution.

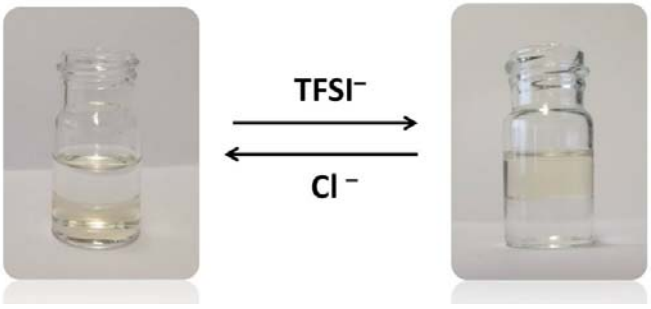

Figure S24. Photographs of the reversible phase transfer of Pd clusters assisted by the cage molecules between an aqueous and EA phases upon anion exchange.

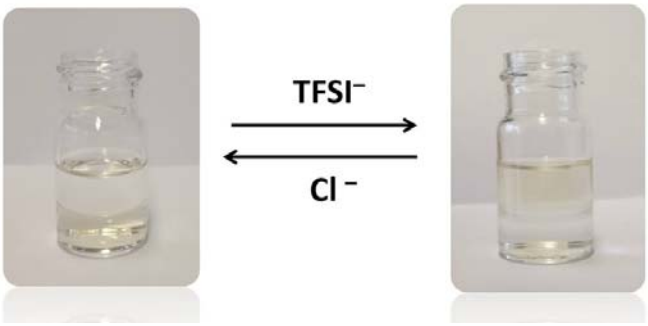

Figure S25. Photographs of the reversible phase transfer of Pt clusters assisted by the cage molecules between an aqueous and EA phases upon anion exchange.

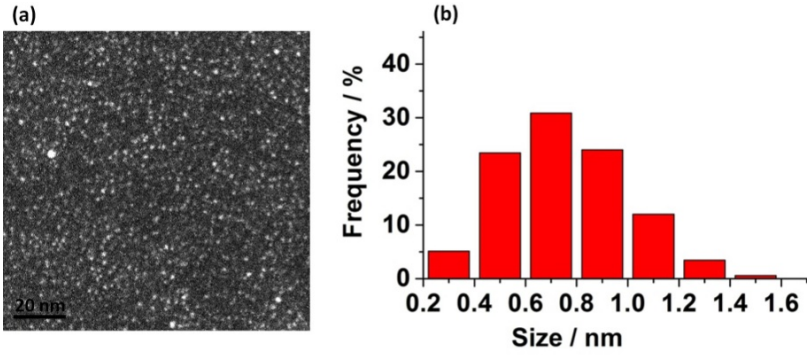

Figure S26. (a) HAADF-STEM image of Pt@I-Cage-Cl catalyst and (b) the corresponding size distribution histogram of Pt clusters (0.75 ± 0.2 nm).

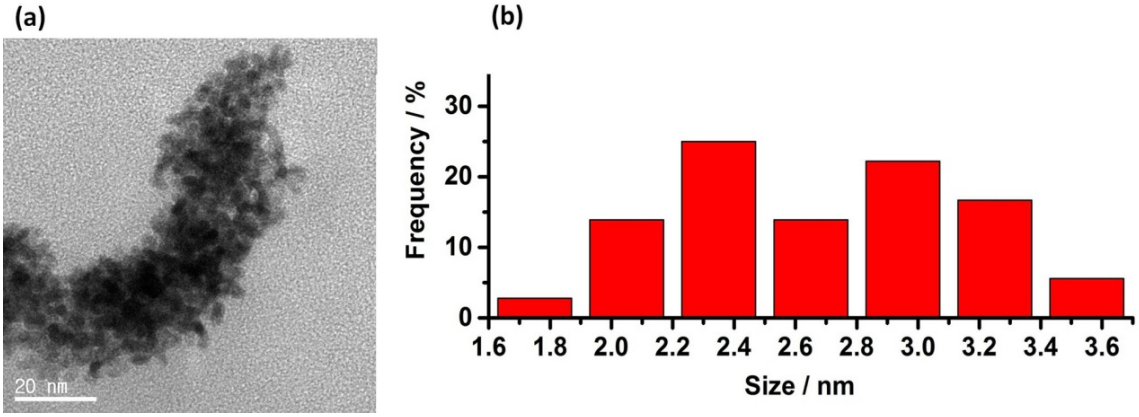

Figure S27. (a) TEM image of Pt/CTAB and (b) the corresponding size distribution histogram of Pt nanoparticles (2.7 ± 0.3 nm).

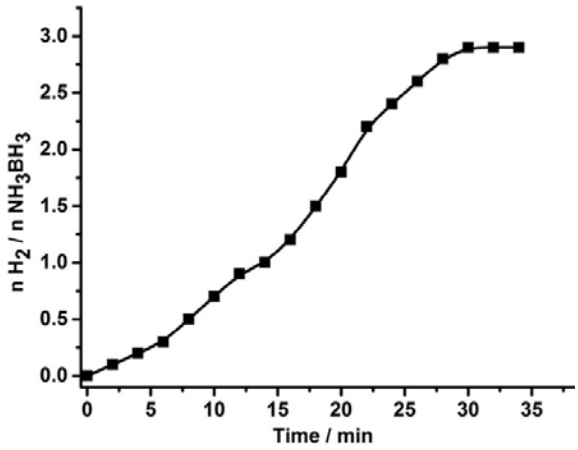

Figure S28. The time course plot of H_2 generation for Pt/CTAB catalyst.

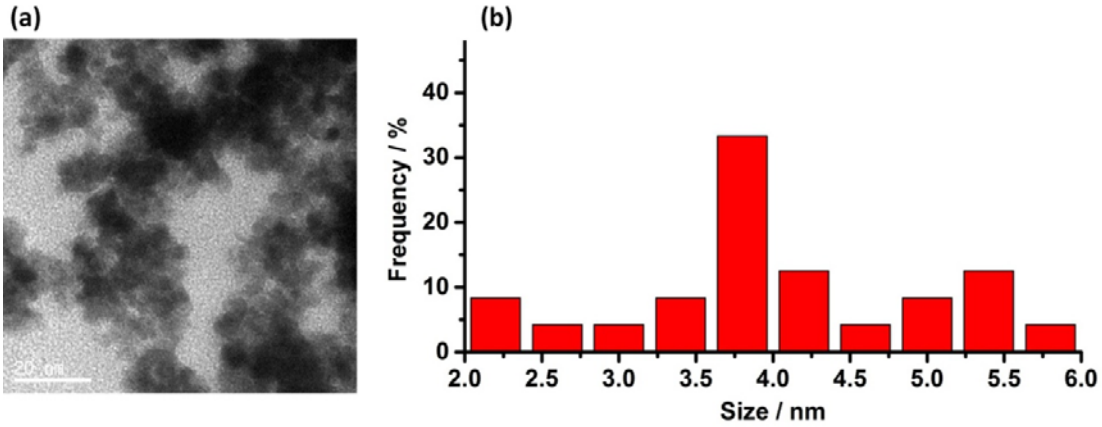

Figure S29. (a) TEM image of Pt/PVP and (b) the corresponding size distribution histogram of Pt nanoparticles (4 ± 0.4 nm).

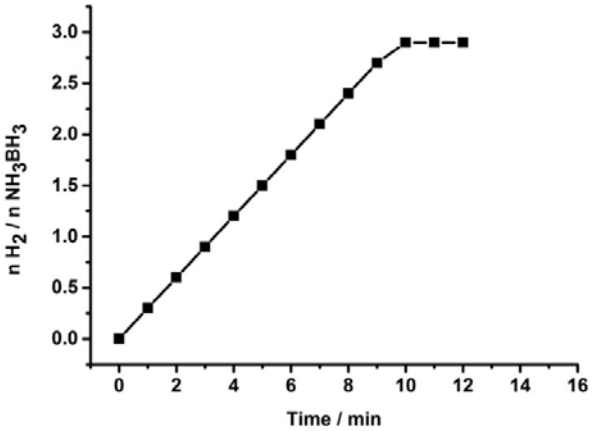

Figure S30. The time course plot of H_2 generation for Pt/PVP catalyst.

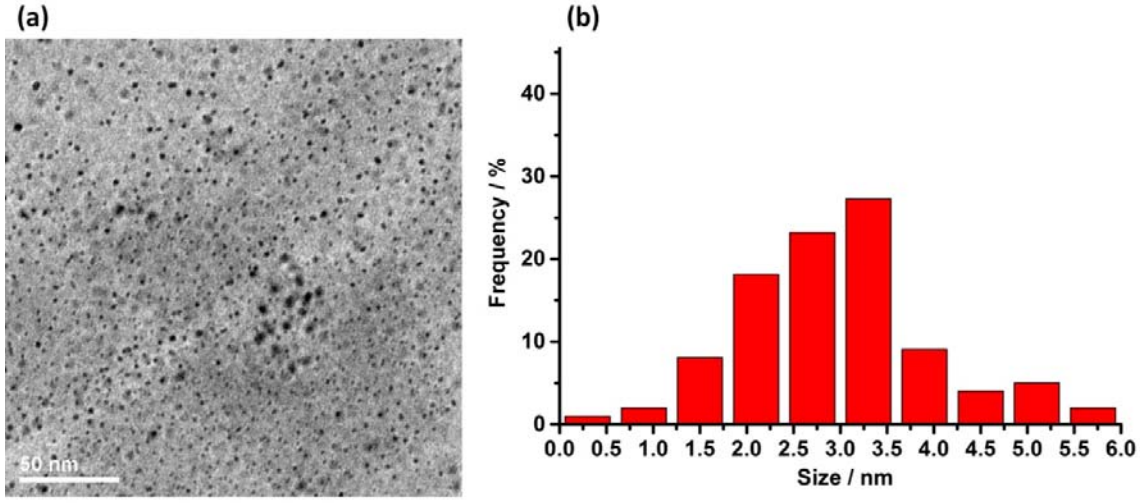

Figure S31. (a) TEM image of Pt/RCC3 and (b) the corresponding size distribution histogram of Pt nanoparticles (3 ± 0.6 nm).

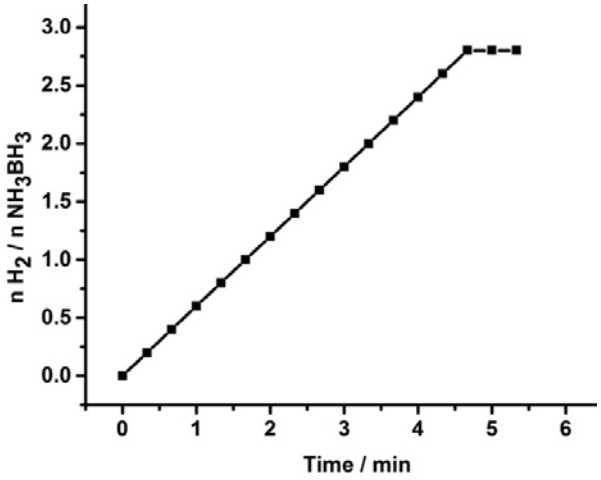

Figure S32. The time course plot of H_2 generation for Pt/RCC3 catalyst.

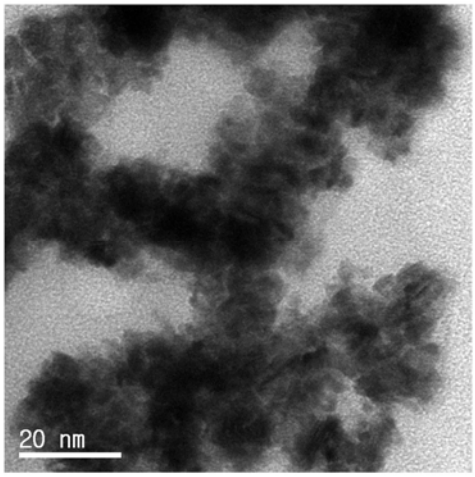

Figure S33. The TEM image of Pt-SP-Free catalyst.

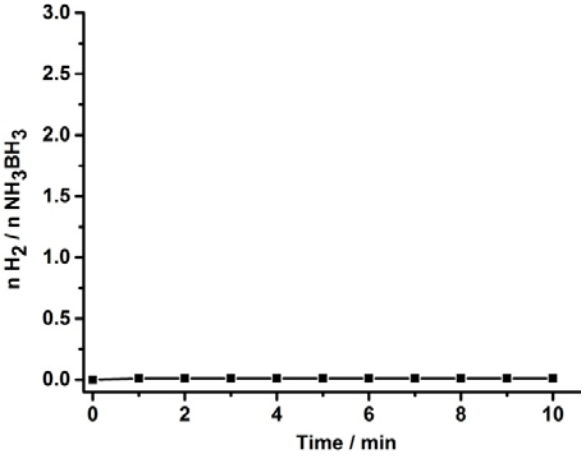

Figure S34. The time course plot of H_2 generation for pure I-Cage-Cl.

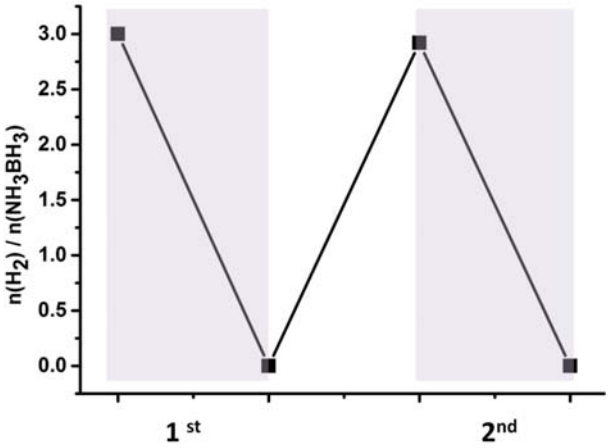

Figure S35. Recyclable AB hydrolysis reaction by Pt@I-Cage-Cl through anion exchange driven phase transfer.

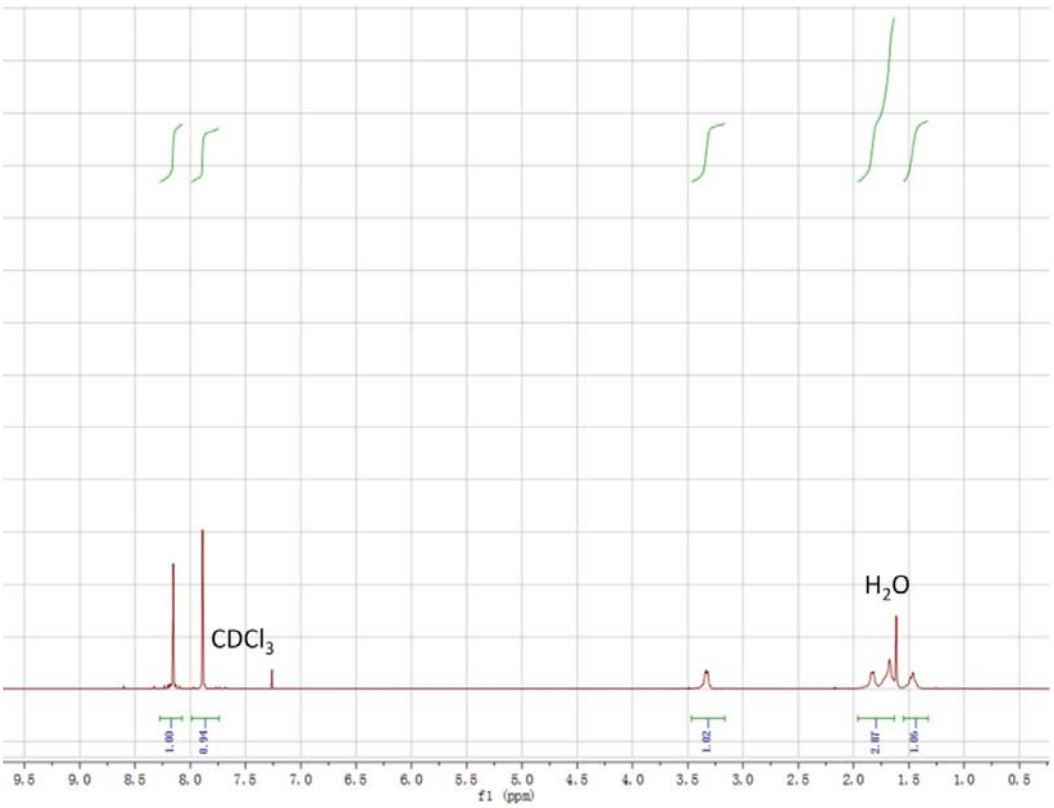

Figure S36. The integration of the ^{1}H NMR spectrum of the CC3 in $CDCl_3$.

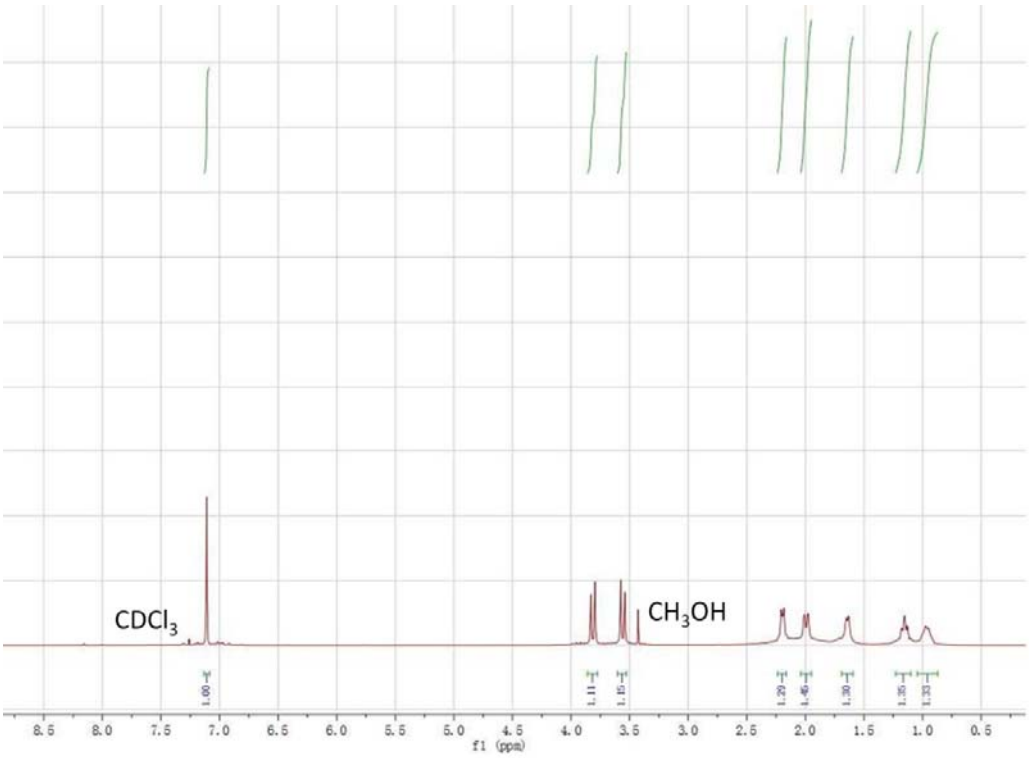

Figure S37. The ^{1}H NMR spectrum of the RCC3 in $CDCl_3$.

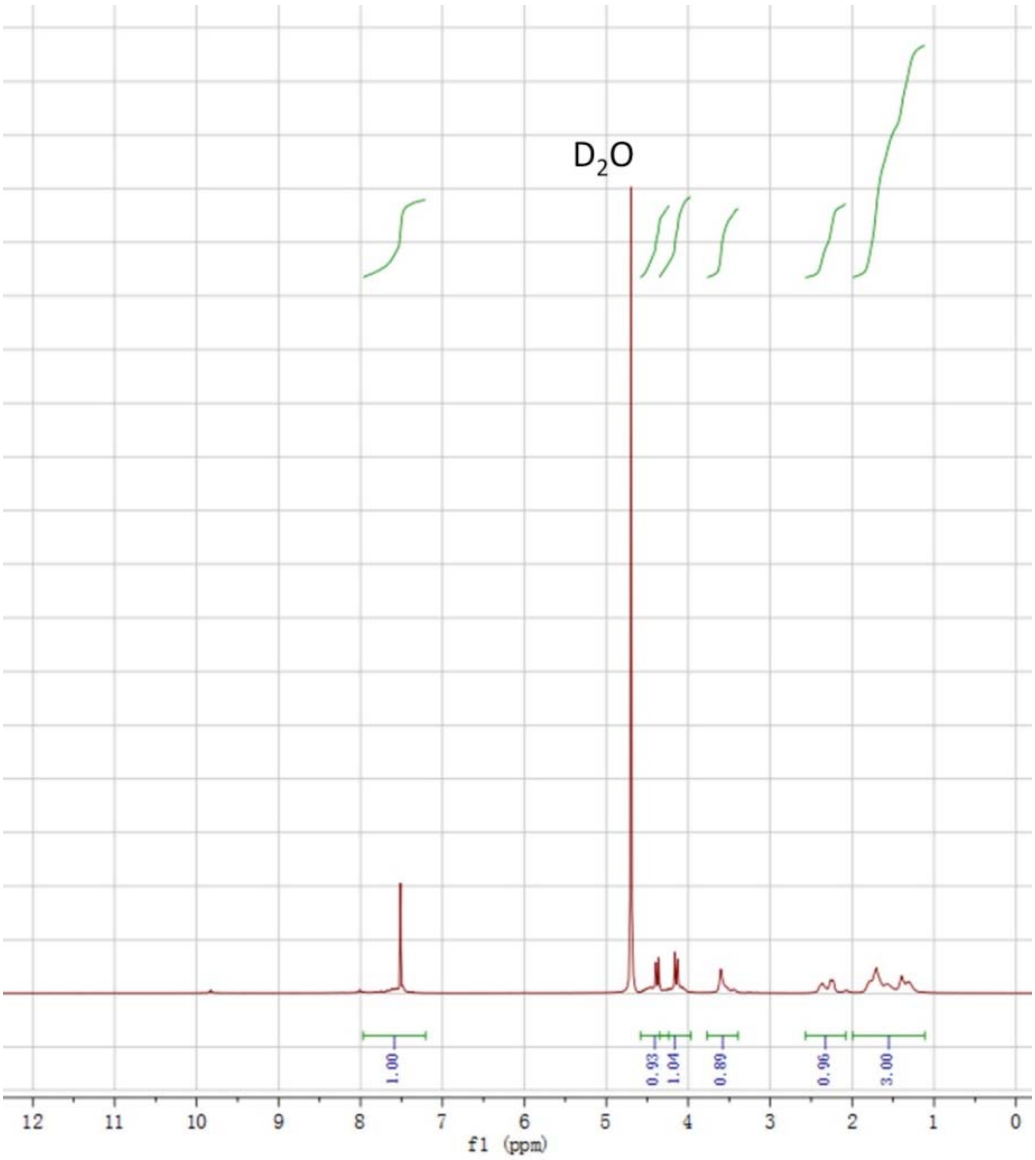

Figure S38. The integration of the ^{1}H NMR spectrum of the I-Cage-Cl in D_2O.

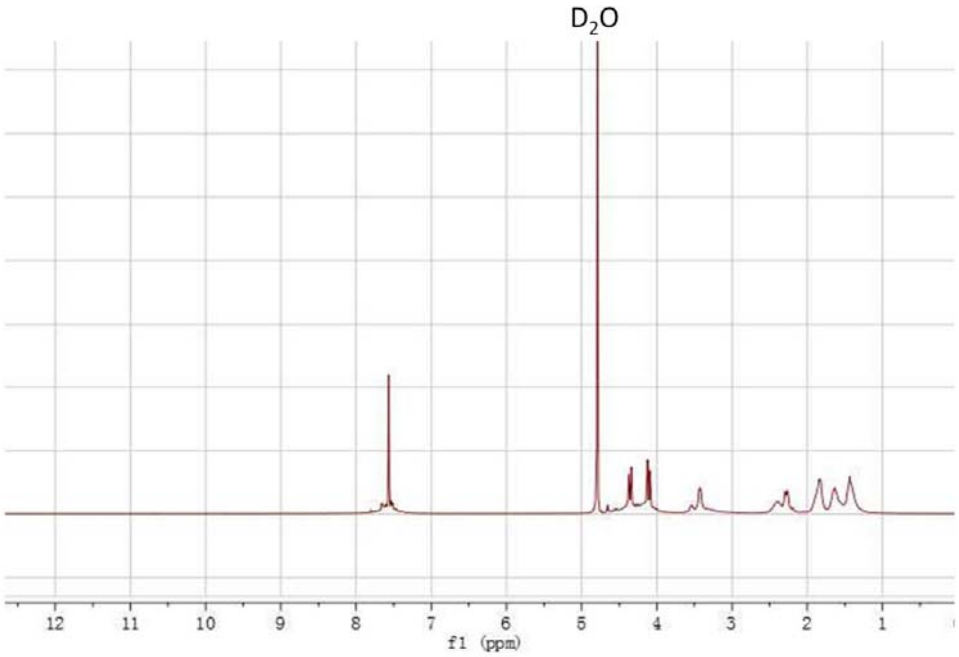

Figure S39. The ^{1}H NMR spectrum of the Pd@ I-Cage-Cl in D_2O.

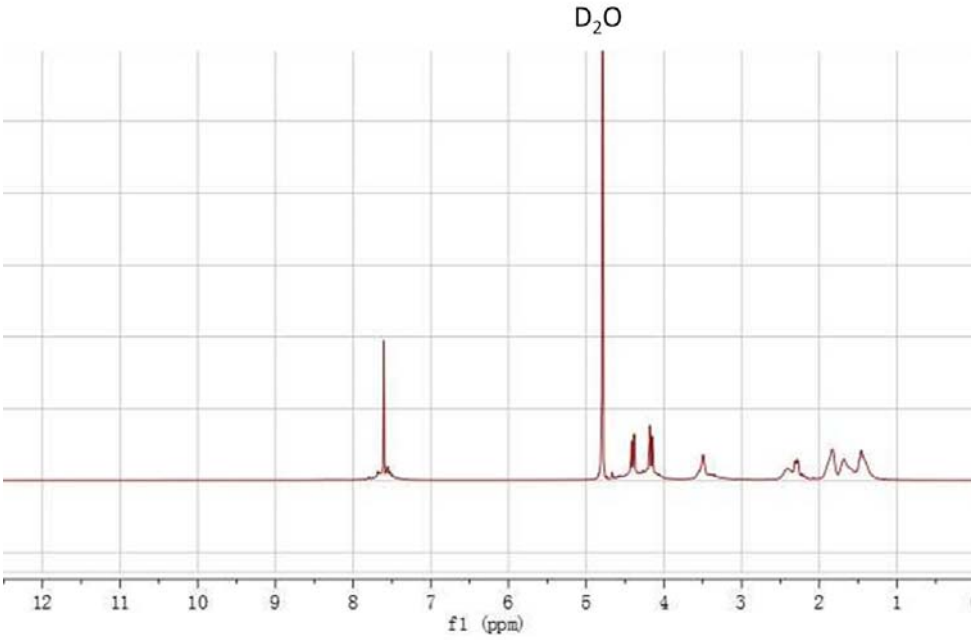

Figure S40. The ^{1}H NMR spectrum of the Pt@ I-Cage-Cl in D_2O.

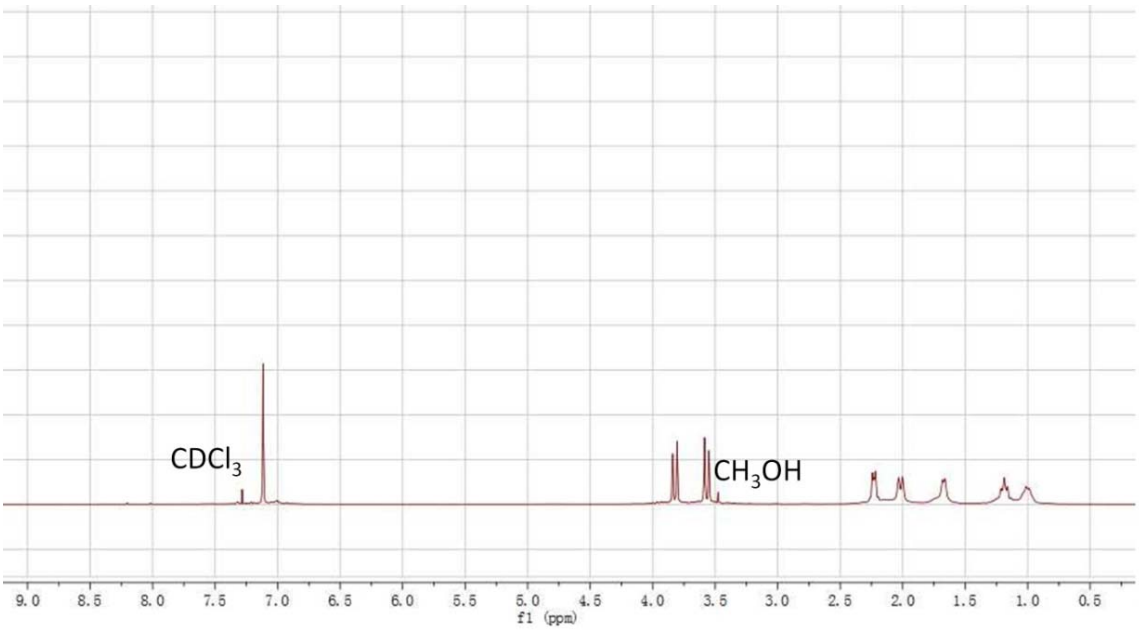

Figure S41. The ^{1}H NMR spectrum of the Au/RCC3 in $CDCl_3$.